

Contents lists available at [ScienceDirect](http://www.sciencedirect.com)

# Mechanical Systems and Signal Processing

journal homepage: [www.elsevier.com/locate/ymssp](http://www.elsevier.com/locate/ymssp)

## A distributed mechanical joint contact model with slip/slap coupling effects

Hamid Ahmadian\*, Mohsen Mohammadali

Center of Excellence in Experimental Solid Mechanics and Dynamics, School of Mechanical Engineering,  
Iran University of Science and Technology, Narmak, Tehran 16844, Iran

### ARTICLE INFO

#### Article history:

Received 8 September 2015

Received in revised form

17 March 2016

Accepted 15 April 2016

#### Keywords:

Contact interface

Friction

Normal load variations

Slip/slap coupling

### ABSTRACT

This paper introduces a zero thickness interface model that considers hysteresis effects in both normal and shear directions of a contact. The model is rate independent and represents coupling effects between normal and shear displacements. Contact effects are included through a segment-to-segment contact model which considers stick, micro-slip, slide and slap behaviors at every point within the contact interface. The model has six parameters and three memory variables without the need for integration during response computations. Behavior of the model is validated using the available mechanical joint records in the literature and it is successfully employed for model identification and dynamic response prediction of an internally resonating test structure with frictional support.

© 2016 Elsevier Ltd. All rights reserved.

## 1. Introduction

Most engineering structures are composed of substructures attached together with mechanical joints such as bolts and rivets. These joints have decisive effect on the assembled system stiffness and often are the main reason for damping and nonlinear response. Consequently, much attention has been paid to modeling of the joints over the past decades [1]. The joint models are essential for studying and prediction of the dynamic response of structures and reduce the need for further experimentations in these studies. The success of these models depends on their ability to predict the relation between the field deformations and the transferred forces properly.

The contact behavior depends on interacting surface properties, loadings and contact region deformations. This behavior is studied from micro-scale [2,3] and macro-scale [1,4] observation points. In micro models, the contact is studied based on asperities shape, size, distribution, mechanical properties, molecular dynamics and statistical parameters. The macro models are not concerned with actual contact mechanics, but are parametric mathematical formulations that can be used for fitting experimentally obtained friction behavior. These investigations are performed in three fields; the first is studying the friction characteristics in contact interface considering variations of the tangential component while the normal force is assumed constant (e.g. Iwan, Valanis and Bouc–Wen models [1]). The application of these models is limited to contacts with simple geometry and negligible normal load fluctuation. In these models the coupling of normal motion and tangential vibration at the interfaces is ignored leading to the symmetry of hysteresis loops. However, in experimental observations asymmetric hysteresis loops are frequently seen [5]. The second field of study considers the behavior of interface in normal

\* Corresponding author.

direction with no frictions in the contact (e.g. Hunt–Crossley and Lankarani–Nikravesh models [6]). The application of this approach is limited to collision of multi-body systems or contacts with perfectly frictionless surfaces. The third field of study focuses on developing a general contact model considering the interaction of normal and tangential vibration at the interface. Song and his colleagues [7] introduced an interface element that accounts for damping due to both vibro-impacts and friction. They used a gap element with linear stiffness and damping in normal direction and Jenkins elements with variable threshold force which is defined based on Coulomb's law in shear direction of contact. Menq and his co-workers [8] used a gap element with linear stiffness in normal direction and a complex slip model in tangential direction to model the contact. The shear stiffness of the model is independent of normal pressure and there is no damping considered in normal direction. Willner [9] presented a general simulation approach for the elasto-plastic contact behavior of rough surfaces based on a half-space model. In his model, normal and tangential stiffness of the contact as well as micro-slip effects depend on contact pressure. A linear relation between slip and tangential force is adopted and the slip threshold displacement is assumed constant; independent of contact normal force. Micro slip regime in the last three-mentioned studies is modeled linearly, therefore to reproduce real behavior of the contact mesh size should be very small.

Moerlooze and his colleagues [2] modeled the contact between two surfaces as the contact of a reduced set of asperities and an elastic non-dissipative counter profile. The local adhesion between the asperity tips and the counter profile, together with the elastic-plastic behavior of the asperities themselves, form the basis for their model. This contribution offers a mean to simulate verity of frictional behavior that is observed in experiments. To use this model, one must discretize the contact with meshes close to the asperies size.

Most of the contact models are deterministic with design variables identified via experiments. Number of the design variables and computational complexity beside the accuracy are other aspects of contact models. Recently, Ruderman and Bertram [10] introduced Modified Maxwell-slip model (MMS) for pre-sliding friction behavior that require two parameters to describe the smooth hysteresis of the pre-sliding friction. The present paper combines the solution of MMS model with empirical relation reported by Etsion and his colleagues [11,12] to relate slip threshold force to normal pressure, leading to a frictional contact model. The proposed contact model employs a Hertzian model with hysteresis properties in normal direction of the contact that is coupled with the suggested friction model. The number of model parameters are reduced by introducing a constant ratio between normal and tangential stiffness of the contact at the initiation of slip [13]. The proposed zero thickness contact model is rate independent with six design and three memory variables that model hysteresis effects and couplings effects between normal and tangential directions of the contact.

The organization of this paper is as follows. In section two the contact model is introduced and its predictions are validated in Section 3 against experimental observations reported in the literature. In section four, an experimental setup with a frictional contact is presented and its equations of motion are developed with special focus on the contact region. The contact region of the experimental setup is modeled using the proposed model of the current paper. The contact model parameters are identified using the experimental recorded response and the resultant model predictions are validated in section five. Finally, section six draws the conclusions.

## 2. Contact model

A conceptual reorientation of frictional contact is shown in Fig. 1. The current study ignores inertial effects of the asperities, and employs a simplified form of the Moerlooze and his colleagues [2] model to describe the contact behavior at the asperities level.

During quasi-static loading, the external normal and tangential loads,  $F_N$  and  $F_T$  respectively, are related to contact loads by

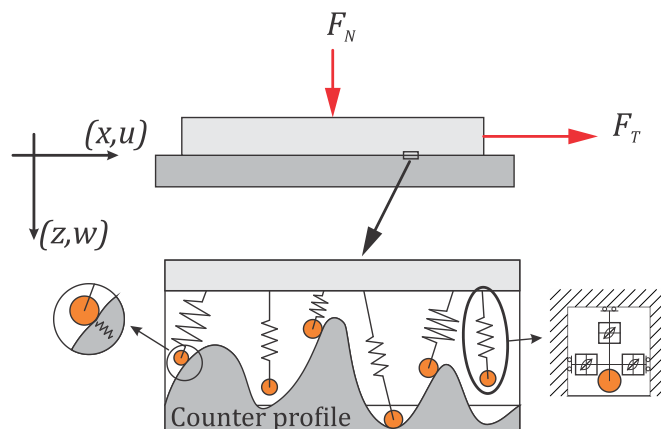


Fig. 1. The contact model introduced by Moerlooze et al. [2].

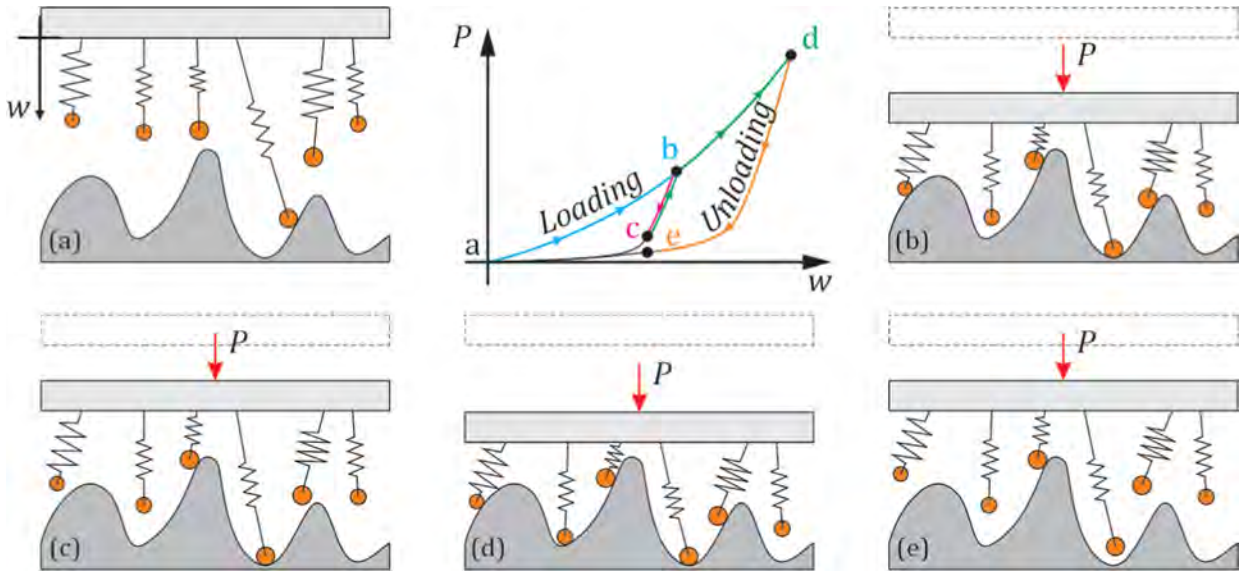


Fig. 2. Hysteresis effects in normal loading; asperities deformation at each point on the load–displacement diagram is shown with the same label.

$$\begin{aligned}
 F_N &= \int P(x)dx, \\
 F_T &= \int Q(x)dx,
 \end{aligned} \tag{1}$$

where  $x$  is the spatial variable,  $P$  and  $Q$  are respectively contact pressure and shear stress, and the integral is defined over the contact region. For convenience the variable  $x$  is dropped hereafter.

### 2.1. Contact motion in normal direction

At the beginning of normal loading as shown in Fig. 2(a), only the highest asperities engage to the counter profile and plastic deformation occurs due to very high local stresses. Increasing the normal load causes more asperities to participate in the contact formation and the local stresses are reduced (Fig. 2(b)). Through unloading, the contact pressure drops according to maximum penetration depth (Fig. 2(c)). During loading phase asperities experience friction, permanent and elasto-plastic deformation, but during unloading phase the contact behaves almost linear with elastic normal contact stiffness [14]. Therefore, the contact pressure during unloading compared with loading phase always has smaller values for the same penetration depth (Fig. 2(c)).

If the contact is reloaded again (with no separation), the pressure rises according to unloading curve until it reaches the loading curve (Fig. 2, loading path from c to b). Beyond this point, the pressure increases according to loading curve shown in Fig. 2 (loading path from b to d) [14]. This behavior is almost rate independent [15,16].

The relation between pressure and normal displacement during loading phase is studied theoretically [17–19] and experimentally [20,21]. These studies confirm a power law function can be used to describe the relationship,

$$P_{\text{loading}} = C_p w^n \tag{2}$$

where  $C_p$  and  $n$  are constant coefficient and  $w$  is the penetration depth. Inspired by MMS model, this paper proposes an exponential decay for the normal pressure during unloading phase and relates the pressure in loading and unloading phases as,

$$P_{\text{unloading}} = P_{\text{loading}} \exp(-k_N(w_{\text{Max}}(x) - w(x))) \tag{3}$$

where  $w_{\text{Max}}$  is the maximum penetration depth and  $k_N$  is a constant that controls the slope of curve during unloading phase. Eq. (3) is valid through unloading phase until the two surfaces are separated or the penetration depth is increased beyond  $w_{\text{Max}}$ .

Based on the reported results by Goerke and Willner [14] for cyclic loading, during reloading phase after separation of contact, the pressure can be described by loading phase again (Eq. (2)). Using a state variable,  $\Delta_N$ , (Eqs. (2) and 3) are combined to define the loading/unloading phases as,

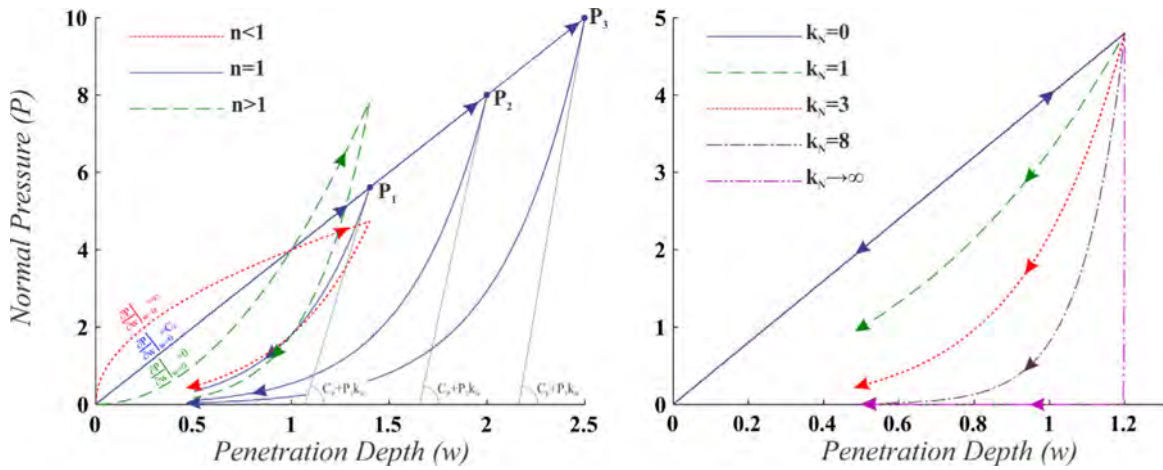


Fig. 3. Effects of  $C_p$ ,  $n$  and  $k_N$  on normal hysteresis loops for the set of trial values given in Table 1.

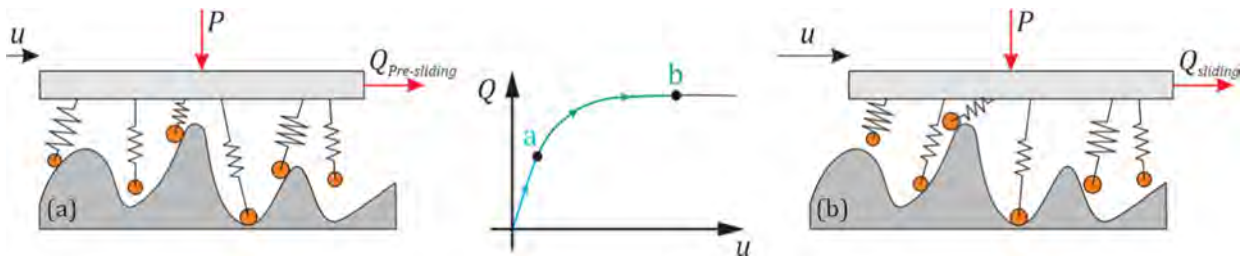


Fig. 4. Hysteresis effects during tangential loading; asperities deformation at each point on the diagram is shown with the same label.

$$P = C_p w^n \Delta_N, \Delta_N = \begin{cases} 1 & 0 < w & \text{Loading} \\ \exp(-k_N(w_{Max} - w)) & 0 < w \leq w_{Max} & \text{Unloading} \\ 0 & 0 \geq w & \text{Separation} \end{cases} \quad (4)$$

The memory variable  $w_{Max}$  is set to zero after each separations. Eq. (4) is valid when there is no slip in the contact. The effect of each parameter in the model behavior is studied as follows.

Eq. (4) describes the relation between normal pressure and normal displacement by three parameters i.e.  $C_p$ ,  $n$  and  $k_N$ . Each of these parameters has a key to produce normal loading hysteresis loops;  $C_p$  is a gain factor that scales the loops,  $n$  has decisive effects on loading and unloading curves, and  $k_N$  controls the slope of unloading curves. Effect of these parameters on the hysteresis loop is depicted in Fig. 3 for a set of trial values. The slope of the hysteresis loop at  $w = w_{Max}$  is

$$\left. \frac{\partial P}{\partial w} \right|_{w=w_{Max}} = \begin{cases} nC_p w^{n-1} & \text{Loading} \\ nC_p w^{n-1} + k_N P & \text{Unloading} \end{cases}, \quad (5)$$

At this point the slope of unloading curve is increased by  $k_N P$  compared to the slope of loading curve.

## 2.2. The Tangential direction

During quasi-static tangential displacement of the contact, engaged asperities to counter profile are deformed elasto-plastically. Some of the asperities start to engage counter profile and some of them break the junction with it as shown in Fig. 4. Increasing the contact tangential displacement  $u$ , the asperities formation of junction and the breaking with the counter profile reaches a steady state condition and the friction force becomes constant. These two are known as pre-sliding and sliding regimes. The pre-sliding regime is almost rate independent but the sliding phase is not; Stribeck and friction lag effects [22] are observed during this regime. These effects may be ignored for small relative speeds  $\dot{u}$ .

Ruderman and Bertman [10] suggested MMS model for relating friction force to the contact tangential displacement. This model is rate independent and describes by a first-order nonlinear differential equation,

$$\dot{Q} = |\text{sgn}(\dot{u})Q_{Max} - Q_0| \dot{u} k_T \exp(-k_T |u - u_0|), \quad (6)$$

where  $Q$  is the friction force,  $Q_{Max}$  is a sliding force,  $k_T$  is a controlling parameter of the overall hysteresis behavior, and  $Q_0$  and  $u_0$  are memory variables that respectively memorize friction force and tangential displacement when motion reversal occurs. In the MMS model  $Q_{Max}$  and  $k_T$  are constants and determine the overall hysteresis behavior.

In order to improve the model, this paper defines friction force of MMS model as,

$$Q = Q_{Max}\Delta_T \tag{7}$$

where  $\Delta_T$  is a state variable preserving the hysteresis behavior varying between  $-1$  and  $1$ .

The nonlinear ODE of the MMS model is solved here in a closed form. Substituting  $Q=Q_{Max}\Delta_T$ ,  $Q_0 = Q_{Max}\Delta_{T_0}$  and  $|u-u_0| = \text{sgn}(\dot{u})(u-u_0)$  in Eq. (6) it is found,

$$\dot{\Delta}_T = |\Omega|\text{sgn}(\dot{u})\frac{d}{dt}[-\exp(-k_T\text{sgn}(\dot{u})(u - u_0))], \tag{8a}$$

$$\Delta_T = |\Omega|\text{sgn}(u)(1-\exp(-k_T\text{sgn}(u)(u - u_0))) + \Delta_{T_0} \tag{8b}$$

where  $\Omega=\text{sgn}(u) - \Delta_{T_0}$ , and  $\Delta_{T_0}$  is a memory variable that memorizes the value of the tangential state variable when motion reversal occurs. If contact is separated and joined again then  $u_0$  and  $\Delta_{T_0}$  are set to  $u$  and  $0$ , respectively. The sliding occurs when  $|\Delta_T|\geq 0.99$ .

The proposed empirical relation by Etsion et al. [11,12] is employed to relate the sliding force to normal pressure of the contact as,

$$Q_{Max} = C_Q P^m \tag{9}$$

where  $C_Q$  and  $m$  are constant variables. Also during loading phase in normal direction, it is shown that the ratio between

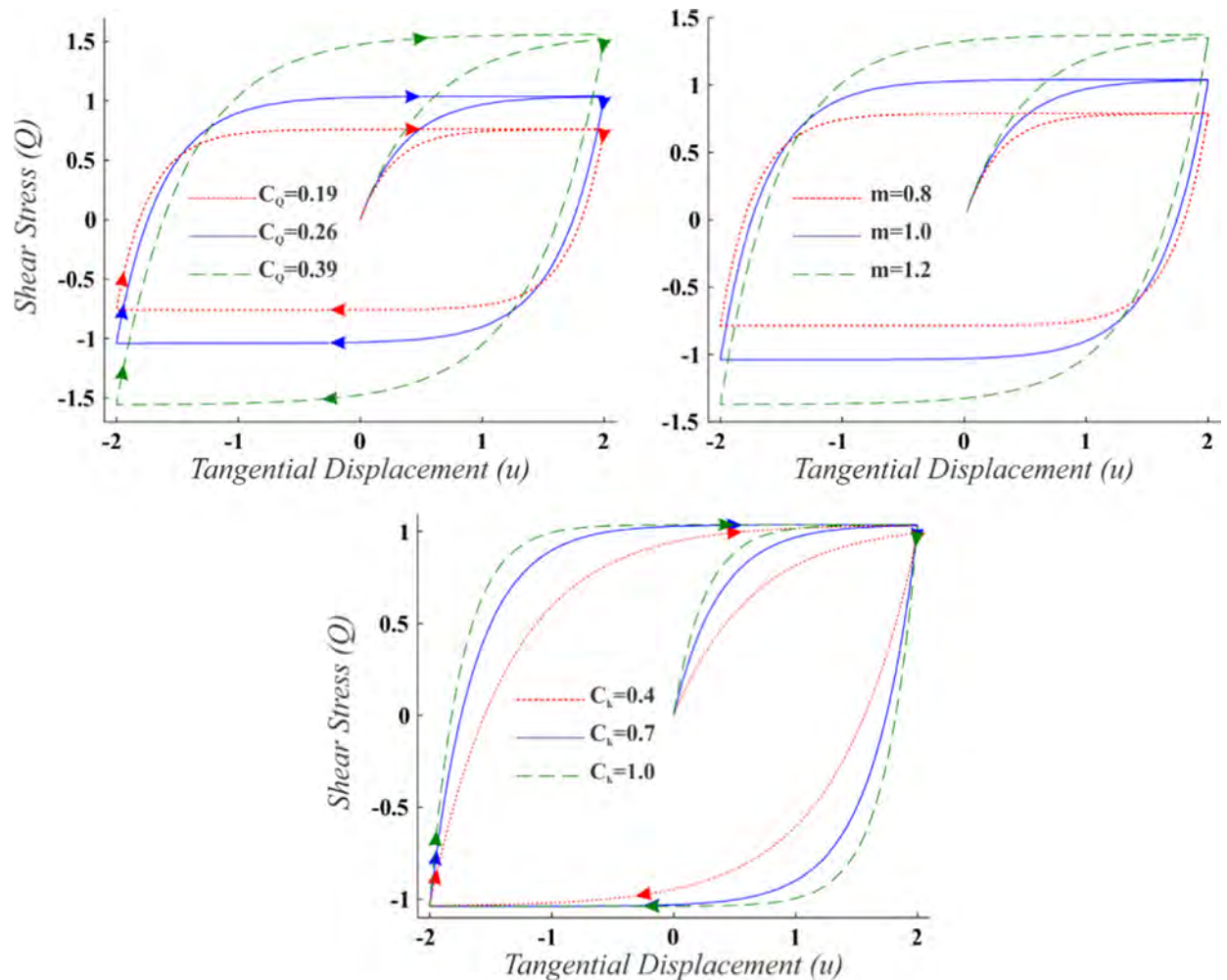


Fig. 5. Influence of  $C_Q$ ,  $m$  and  $C_k$  on tangential hysteresis loops for the set of trial values given in Table 1 when  $P=2$ .

tangential stiffness and normal stiffness of the contacts is constant [13]. Using this fact one may obtain,

$$C_k = \frac{dQ/du}{dP_{loading}/dw} = k_f C_Q W^{n(m-1)+1} C_P^{m-1} n^{-1} \tag{10}$$

where  $C_k$  is a constant. Solution of Eq. (10) for  $k_f$  leads to

$$k_f = \frac{n C_k C_P^{1-m}}{C_Q W^{1-n(1-m)}} \tag{11}$$

The presiding displacement is inversely proportional to  $k_f$ . Furthermore, by increasing the penetration depth, the presiding displacement increases. Therefore, the power of penetration depth in Eq. (11) is always negative (i.e.  $n(1 - m) < 1$ ). Incorporating Eqs. (8, 9) and (11) into Eq. (7), the friction force is defined as,

$$Q = C_Q P^m \Delta_T, \Delta_T = |\Omega| \text{sgn}(u) (1 - \exp(\frac{n C_k C_P^{1-m}}{C_Q W^{1-n(1-m)}} \text{sgn}(u)(u_0 - u))) + \Delta_{T_0} \tag{12}$$

The friction and normal forces in the contact have coupling effects; Eq. (12) defines only a part of this effect, namely the effect of normal force on the frictional force.

One may observe the role of each parameter in tangential motion using the following study. Eq. (12) describes the relation between tangential stress and displacement by three parameters (i.e.  $C_Q$ ,  $m$  and  $C_k$ );  $C_Q$  acts like the friction coefficient and scales the hysteresis loops in tangential direction, but the slope of the hysteresis loop at initiation of slip and when motion reversal occurs (i.e.  $u = u_0$ ) is independent of  $C_Q$  (see Eq. (13)). The other parameter  $m$  is always close to one and has an important role in relating the sliding force to normal pressure. The slope of the hysteresis loop in the tangential direction in pre-sliding regime mainly control by  $C_k$ ,

$$\frac{\partial Q}{\partial u} = |\Omega| P^m \frac{n C_k C_P^{1-m}}{W^{1-n(1-m)}} \exp(\frac{n C_k C_P^{1-m}}{C_Q W^{1-n(1-m)}} \text{sgn}(u)(u_0 - u)) \tag{13}$$

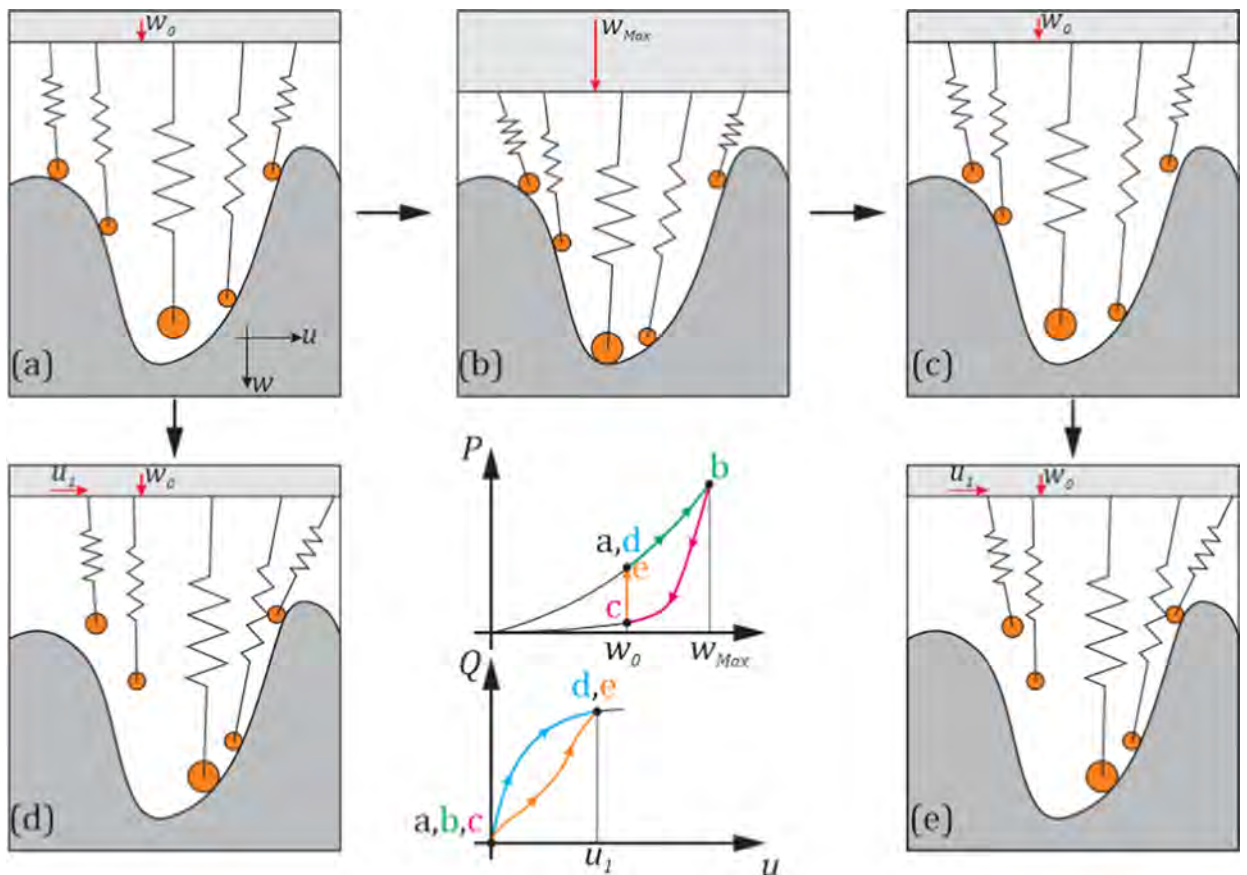


Fig. 6. A simplified lift-up model; asperities deformation at each point on the diagram is shown with the same label.

Fig. 5 shows the impact of these parameters on the hysteresis loops for a set of trial values.

2.3. Effect of tangential motion on normal forces

Few studies consider the effect of tangential displacement on normal field parameters especially under cyclic loading; most available contact models ignore this coupling. Among the few, Al-Bender and his coworkers [23] reported lift-up effect. They performed dry, pre-sliding rubbing experiments that show regular, relative normal displacement associated with the tangential motion. It is believed there is another phenomenon that can cause lift-up effect during cyclic loading in normal and tangential directions.

Considering the loading sequence depicted in Fig. 6 the contact is loaded to reach penetration depth of  $w_0$  (Fig. 6(a)) and with more loading to penetrate depth of  $w_{Max}$  (Fig. 6(b)). Then the normal load is decreased to reach the penetration depth of  $w_0$  again through unloading curve (Fig. 6(c)). Finally, both conditions (a) and (c) are loaded tangentially until sliding occurs as they labeled with (d) and (e) respectively. Comparing condition (c) with (a), some of asperities are disengaged from counter profile due to the plastic and elasto-plastic deformations [16]. In condition (c) for the constant penetration depth of  $w_0$ , when tangential displacement occurs, it is expected that some of disengaged asperities engage to counter profile again and climb up of its hills. Consequently, the contact pressure at this instant starts to increase until sliding occurs (i.e.  $\Delta_T \geq 0.99$ ), while all engaged asperities experience the same condition of (d) the contact pressure reaches the value of loading phase.

Suggesting a linear relation between transmission from no-slip to sliding and moving from unloading to loading curve, one may define a modified pressure state variable for coupling effect of normal and tangential motion in the following form,

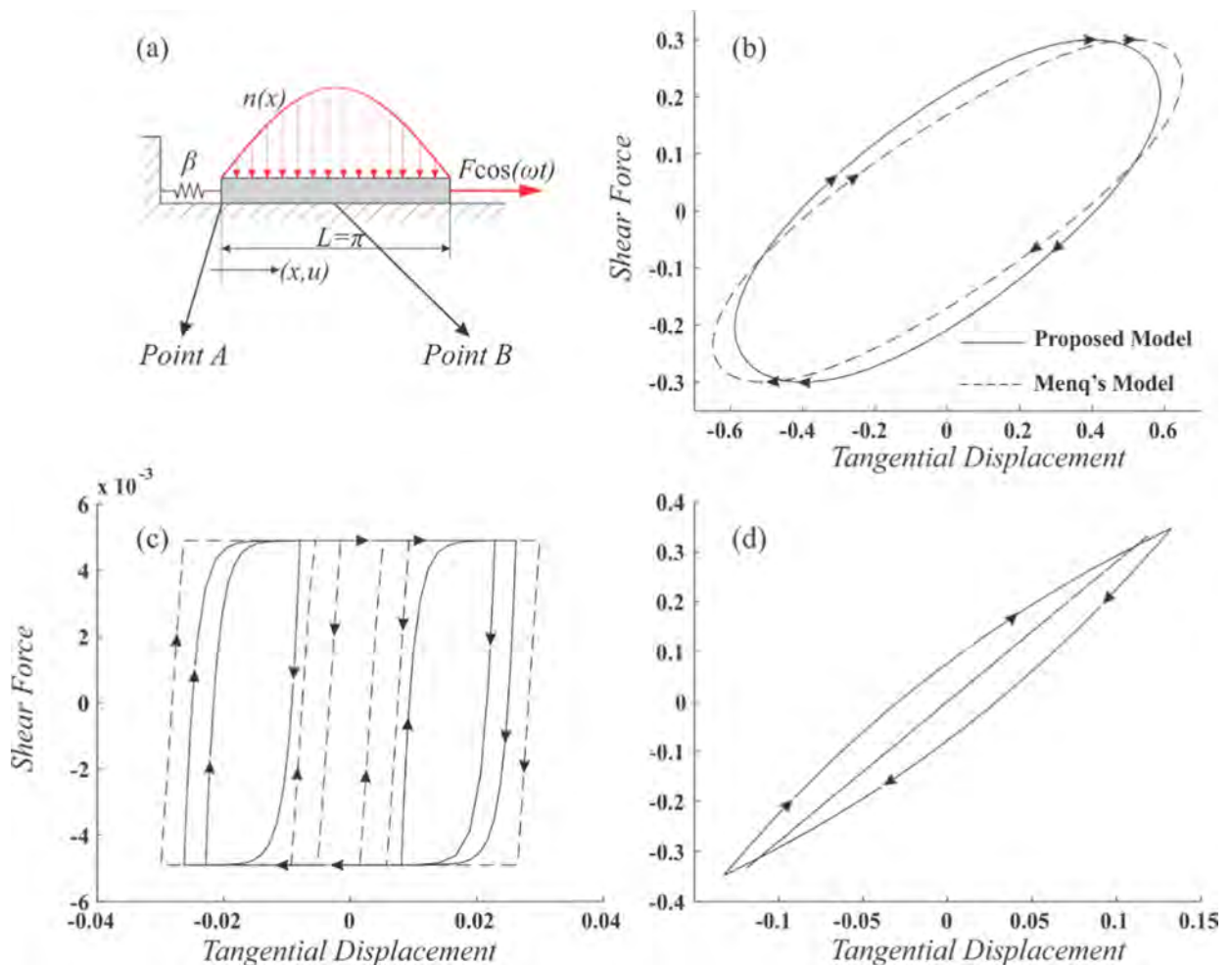


Fig. 7. (a) A rod resting of frictional surface (b) external load hysteresis loop (c) hysteresis loop at point A (d) hysteresis loop at point B.

**Table 1**

Trial values selected for design variables.

Proposed model	$C_p$	$C_k$	$C_Q$	$n$	$m$	$k_N$
Menq model	4	0.7	0.26	1	1	0
	$k_v$	$k_u = C_k \times C_p$	$\mu$	N/A		
	4	2.8	0.26			

$$P = C_p W^n \Delta_p, \quad \Delta_p = \Delta_N + (1 - \Delta_N) |\Delta_T|, \quad \Delta_N = \begin{cases} 1 & 0 < w \\ \exp(-k_N(w_{Max} - w)) & 0 < w \leq w_{Max} \\ 0 & 0 \geq w \end{cases} \begin{matrix} \text{Loading} \\ \text{Unloading} \\ \text{Separation} \end{matrix} \quad (14)$$

$\Delta_p$  varies between 0 to 1. When sliding occurs, memory of loading history in normal direction is refreshed by letting,  $w_{Max} = w \quad |\Delta_T| \geq 0.99$ . (15)

The replacement causes 1% jump in  $\Delta_p$  at most which is negligible. One should note the state variable  $\Delta_N$  models hysteresis effects due to pure normal motions, but  $\Delta_p$  considers both normal and tangential motion effects.

**3. The contact model performance validation**

The proposed contact model has six design variables (i.e.  $n, m, k_N, C_p, C_Q$  and  $C_k$ ) and the contact deformations are related to the contact loads using three memory variables (i.e.  $w_{Max}, u_0$  and  $\Delta_{T_0}$ ) as described in (Eqs. (12) and 14). One may ignore some effects in the contact by setting the values of the related parameter appropriately. As an example one may reduce the number of model design variables to three by ignoring the energy dissipation due to the contact normal motion ( $k_N=0$ ) and considering linear relations in (Eqs. (2) and 9) (i.e.  $n = m=1$ ). These considerations simplify the proposed model and bring it close to the contact model suggested by Menq and his colleagues [8] with some superior properties. The rod resting on a frictional surface shown in Fig. 7 is selected as a case study and the contact interface is modeled both by the Menq model and simplified form of the proposed contact model (i.e.  $n = m = 1$  and  $k_N=0$ ). Equation of motion for the rod is,

$$\frac{\partial^2 u}{\partial t^2} - \frac{\partial^2 u}{\partial x^2} + Q = F \cos(\omega t) \delta(x - L) - \beta u \delta(x) \quad (16)$$

where  $\omega = 1, t, Q, F = 0.2, \beta = 0.01$  and  $\delta$  are non-dimensional excitation frequency, time, friction force, external force amplitude, lumped stiffness and Dirac delta function, respectively. Table 1 shows selected trial values for the contact models, where  $k_v, k_u$  and  $\mu$  are normal stiffness, tangential stiffness and friction coefficient in Menq Model.

The preload distribution is considered time invariant and in the form of  $n(x) = \sin(x)$  during tangential loading. The response of the system is calculated using harmonic balance method in conjunction with modal expansion technique. As shown in Fig. 7(b) the predicted displacements of both models are very close.

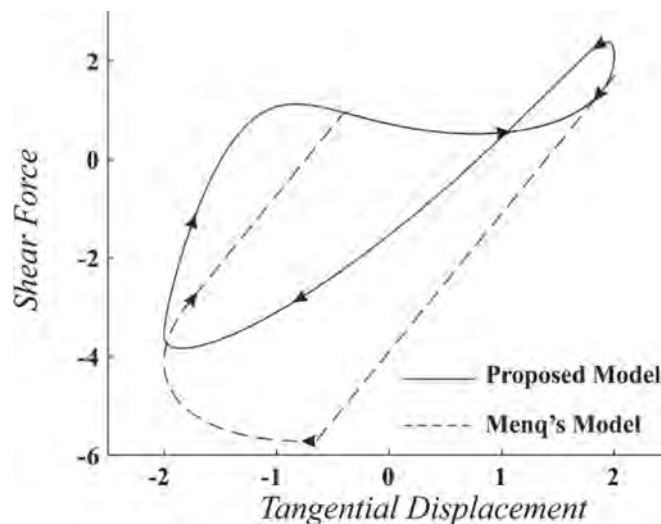


**Fig. 8.** Tangential hysteresis curve for the selected trial values of Table 1  $u=2\sin(t + 5\pi/8)$  and  $w=3 + 2.5\sin(t)$ .

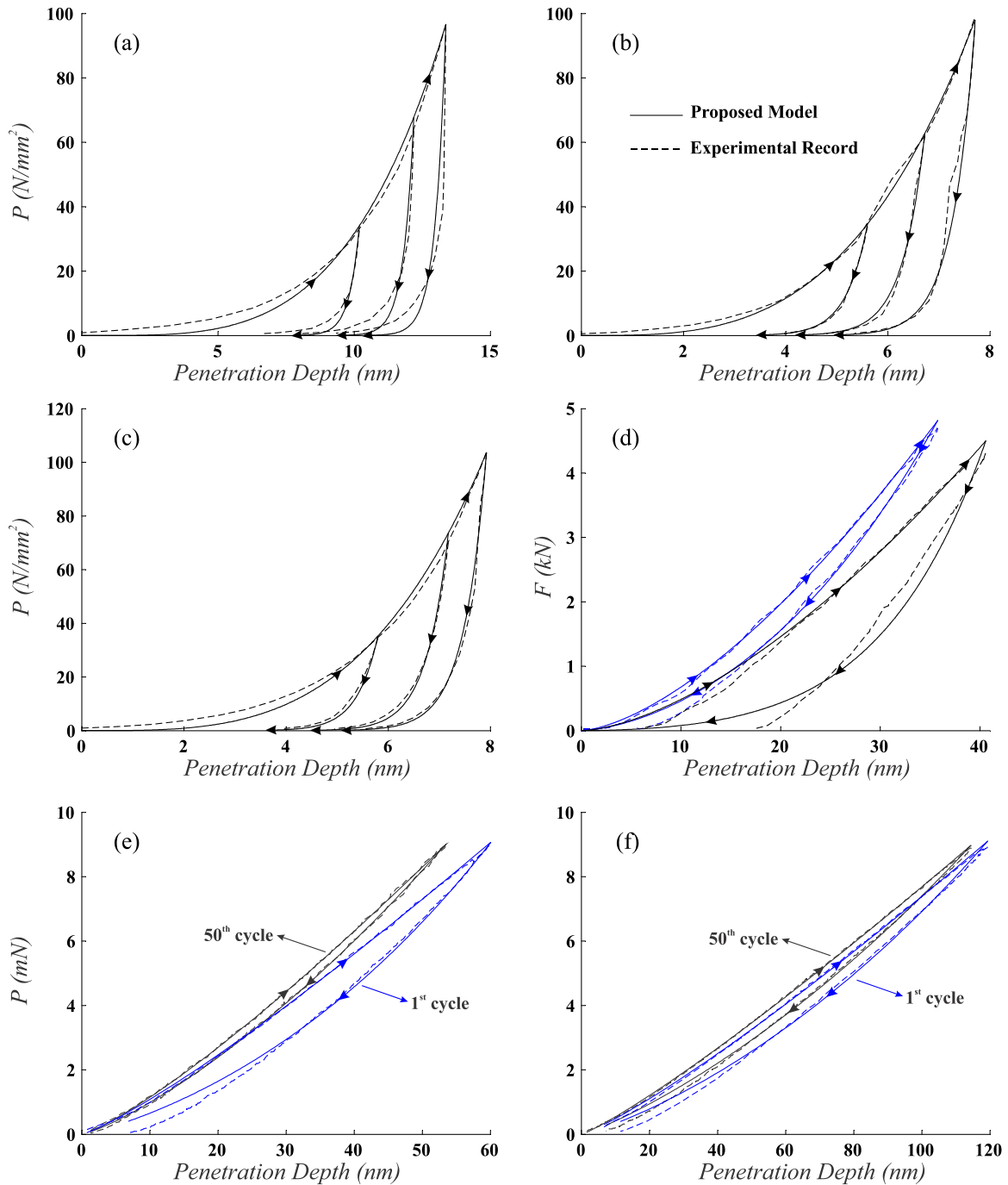


**Fig. 9.** Hysteresis loop in normal direction (a) spark-eroded and (b,c) sand-blasted aluminum specimens which the parameters are identified using the largest loop and small loops are regenerated by the identified parameters [14] (d) impact force [24] (e,f) effect of cyclic loading, the model fitted on each cycle individually [25].

The advantages of the proposed model compared to Menq's model are as follows. The sliding forces in both models are equal for the same normal load (Fig. 7(c)), but Menq's model does not consider energy dissipation until it reaches the sliding condition. This is in contrast with experimental observations (known as micro-slip mechanism) while the proposed model produces more realistic damping mechanism compared to the Menq's model as seen in (Fig. 7(d)). Another reason for justifying the superiority of the proposed model is its capability in generating internal loops in the presence of normal load variation observed in experimental measurements [5]. This capability is shown in Fig. 8 while the other model cannot predict such an effect.

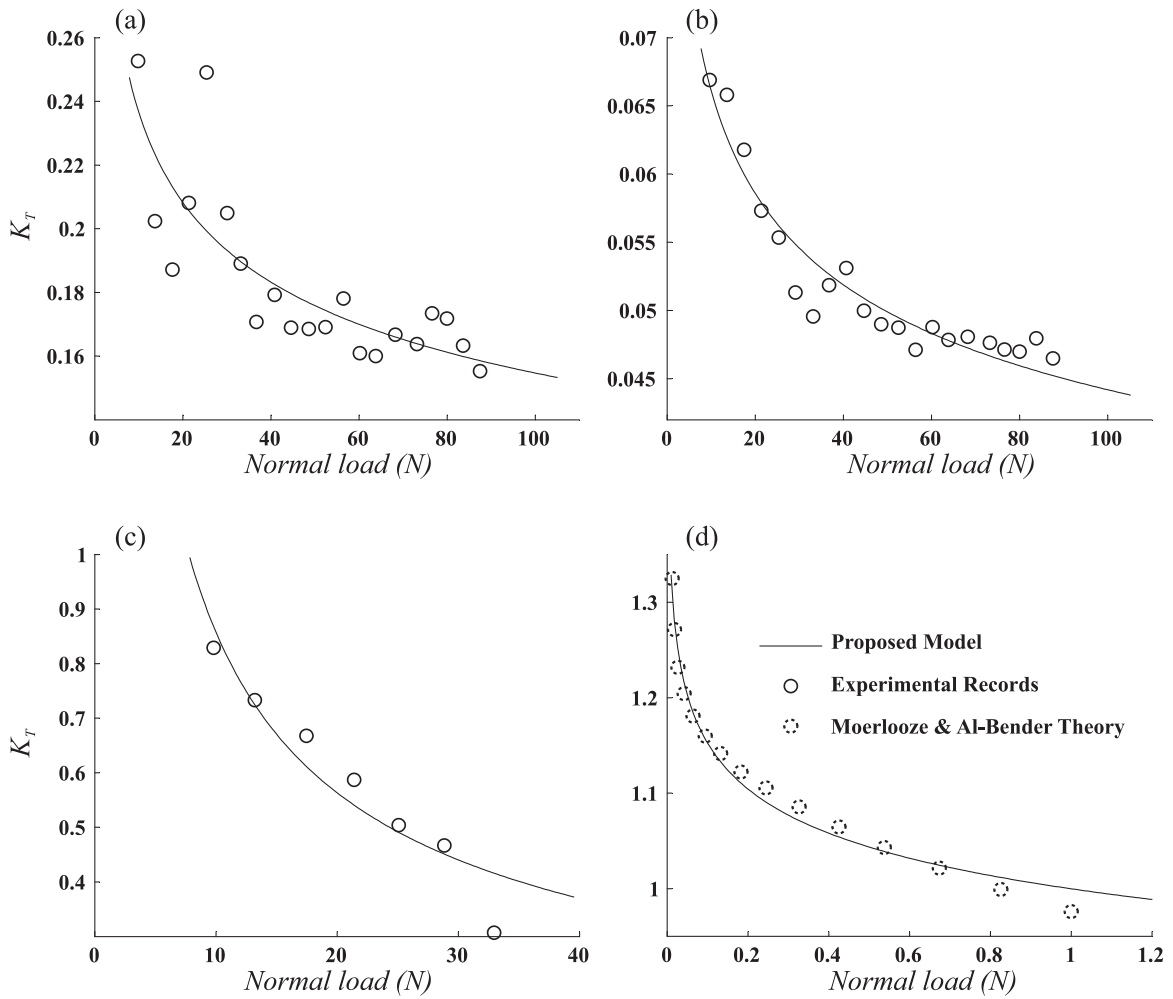


**Fig. 10.** Evaluation of  $k_T$  as function of normal load provided in [26] (a) steel on PET (b) PET on PET (c) brass on steel (d) Al-Bender and Moerlooze theoretical model.

To demonstrate further capabilities of the proposed model, its predictions are validated against available experimental records in the literature. Willner and Goerke [14] studied loading curve of contacts under quasi static compression. The asperities deformation of aluminum test specimens are almost plastic in their study. Zhang and Sharf [24] recorded the

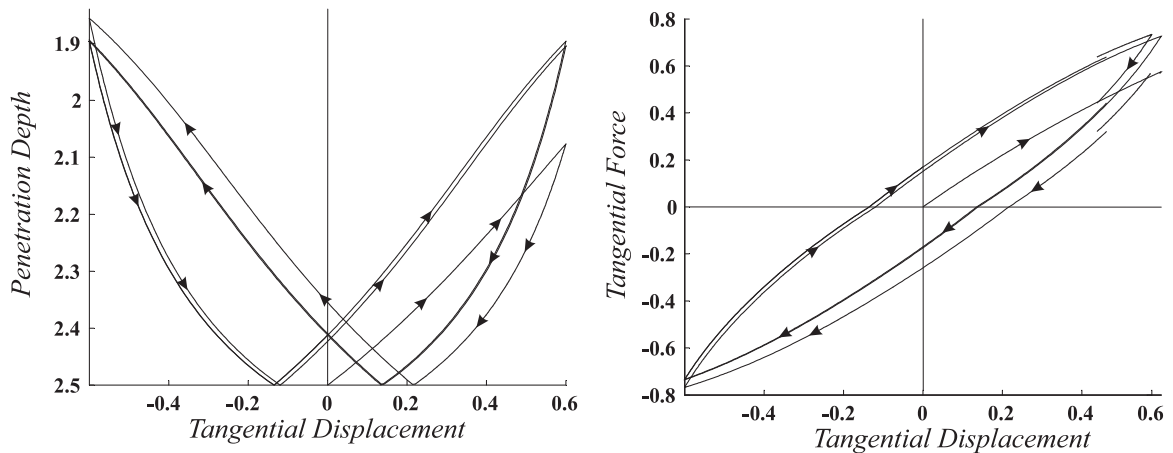


**Fig. 11.** Lift up effect predicted by the proposed model (constant normal load).



plastic and nearly elastic load-displacement curves. In addition, the model successfully predicts the inner loops shown in Fig. 9(a)–(c).

Moerloozee and Al-Bender [26] experimentally investigated the relation between the normal load and the friction force during the pre-sliding regime up to the point of sliding. They used a simple form of Eq. (12) (by selecting  $\text{sgn}(\dot{u})=1$  and  $\Delta\tau_0=0$ ) to fit the experimental records of friction force versus tangential displacement under various normal loadings. The identified value

of  $k_T$  in their study is employed here to examine the validity of Eq. (11) and the outcomes are shown in Fig. 10. The parameters of Eq. (11) are identified by minimizing the difference between model predictions and measured values using least squares technique. As explained in previous section, the proposed model also shows the lift up effect during the pre-sliding shown in Fig. 11.

#### 4. Implementation of the model in a continuous media

The contact model developed in Section 2 is used here to model a beam with frictional contact interface support. The interface region has a considerable area compared to the beam size and is modeled as a continuous media. The parameters of contact interface namely  $n$ ,  $m$ ,  $C_p$ ,  $C_Q$ ,  $C_k$  and  $k_N$  are selected as design variables and their values are obtained by minimizing the difference between the experimental observations and the model predictions.

##### 4.1. The experimental observations

The aluminum beam shown in Fig. 12, resting on a steel frictional support at one end and free on the other side, is employed as another experimental case study. A constant normal preload at the

support is provided by suspended mass blocks. The dynamic response of the system becomes nonlinear when the motion amplitude is large enough to cause slip and vibro-impacts at the support. The system is excited at point E via an electromagnetic shaker and the response is recorded at point 7 shown in Fig. 12. A laser Doppler vibro-meter is employed to record velocities of the beam at points 1 to 7. The response of the system changes slightly due to perturbation in installation and initial conditions. To overcome these problems, the system is first excited by largest excitation level then the level is decreased in order to reach minimum level, unceasingly. Knowing the softening nature of the contact, the frequency responses (FRs) are achieved by sweeping excitation frequency downward from 40 Hz. The resolution of FRs is increased around the natural frequencies in three steps. To ensure removal of all unwanted initial condition the excitation is started from 40 Hz in all refinement steps. At each frequency steady-state responses is recorded and resonances are found by accuracy of 0.01 Hz. At resonance frequencies, a single harmonic force is applied to the beam by using a shaker controller to guarantee that all observed nonlinear responses are due to structure not the shaker effects.

The frequency responses of the system at nine excitation levels are measured. The excitation frequencies and amplitudes are reported in Table 2 and the resultant frequency responses are shown in Fig. 13.

##### 4.2. Continuous model of beam with frictional support

The equations of motion of the beam with the displacement field  $\mathbf{q} = \{u(x), \phi(x), w(x)\}^T$ , representing axial, rotational and lateral of beam motions, in a non-dimensional form are:

$$(\mathbf{I} + \delta(x - L_E)\mathbf{M})\ddot{\mathbf{q}} + (1 - ih)\mathbf{K}\mathbf{q} + \mathbf{f}_{nl} = \mathbf{f}_E\delta(x - L_E) + \mathbf{f}_{E_0}, \quad \mathbf{L}\mathbf{q} = \mathbf{0} \quad x = 0, L. \quad (17)$$

The mass distribution of the beam in normalized form is an identity matrix,  $\mathbf{I}$ ,  $\mathbf{M}$  introduces the mass effects of the force transducer, the operator  $\mathbf{L}$  enforces the boundary conditions,  $i=\sqrt{-1}$  is unit imaginary and  $h$  is the beam material hysteretic damping coefficient. The stiffness and boundary condition operators of the system are:

**Table 2**  
Resonance data extracted from experimental measurements

Load case #	1	2	3	4	5	6	7	8	9
Resonance frequency (Hz)	42.48	42.41	42.38	42.32	42.24	42.11	42.01	41.80	41.69
Force amplitude (mN)	121	170	198	217	246	278	318	364	384

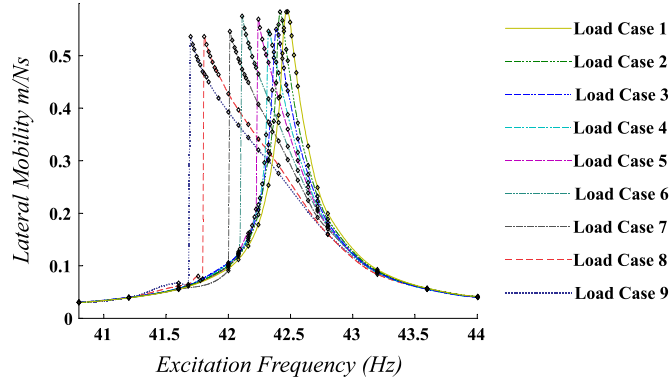


Fig. 13. Measured frequency responses at different excitation levels, ◇ measured frequencies.

$$\mathbf{K} = \begin{bmatrix} -\frac{\partial^2}{\partial x^2} & 0 & 0 \\ 0 & -\frac{\partial^2}{\partial x^2} + \kappa & +\kappa \frac{\partial}{\partial x} \\ 0 & -\kappa \frac{\partial}{\partial x} & -\kappa \frac{\partial^2}{\partial x^2} \end{bmatrix}, \quad \mathbf{L} = \begin{bmatrix} \frac{\partial}{\partial x} & 0 & 0 \\ 0 & \frac{\partial}{\partial x} & 0 \\ 0 & \kappa & \kappa \frac{\partial}{\partial x} \end{bmatrix}, \quad (18)$$

where  $\kappa=0.331$  is the shear correction factor of the beam cross section. The nonlinear restoring forces are:

$$\mathbf{f}_{nl} = \{Q, 3Q, P\}^T (H(x) - H(x - L_c)), \quad (19)$$

where  $H(x)$  is Heaviside function,  $Q$  and  $P$  are the contact tangential and normal loads defined in (Eqs. (12) and 14). The external forces are defined as:

$$\begin{aligned} \mathbf{f}_E &= \{0, 0, F_E \cos(\omega t)\}^T, \\ \mathbf{f}_{E_0} &= \{0, 0, F_0\}^T (H(x) - H(x - L_c)), \end{aligned} \quad (20)$$

where  $F_E$  is the excitation force amplitude and  $F_0$  is the constant preload at the contact interface region.

The steady state solution of Eq. (17) with the period of  $T=2\pi/\omega$  is expanded using  $m$  harmonic terms,

$$\mathbf{q} = \sum_{j=0}^m (\psi_j \cos(j\omega t) + \varphi_j \sin(j\omega t)), \quad x_j = \psi_j + i\varphi_j, \quad \mathbf{f}_{x_j} = (1 + \text{sgn}(j)) \frac{\omega}{2\pi} \int_0^{2\pi/\omega} \mathbf{f}_x e^{ij\omega t} dt \quad X = nl, E \quad (21a)$$

leading to,

$$\begin{aligned} (- (j\omega)^2 \mathbf{I} + \delta(x - L_E) \mathbf{M}) + (1 - ih) \mathbf{K} \chi_j + \mathbf{f}_{nlj} &= \mathbf{f}_{Ej} \delta(x - L_E) \quad j = 1, 2, \dots, m, \\ \mathbf{K} \chi_0 + \mathbf{f}_{nl0} &= \mathbf{f}_{E0} \quad j = 0, \\ \mathbf{L} \dot{\chi}_j &= 0 \quad x = 0, L \end{aligned} \quad (21b)$$

The deformation field is partitioned into two regions with subscripts  $\alpha$  and  $\beta$ , which stand for master and slave regions, respectively. The master region experience nonlinear restoring forces, and linear restoring forces drive the slave region,

$$\mathbf{f}_{nl} = \begin{cases} \mathbf{f}_{nl_\alpha} \neq 0 & x_\alpha \in x < L_c \\ 0 & x_\beta \in x > L_c \end{cases} \quad (22)$$

The problem is now reduced using the authors suggested method [27] for dynamic problems with local nonlinearities to the master region. Consequently, Eq. (21b) can be divided into respected master and slave regions (see Fig. 12) as,

$$\begin{aligned} (- (j\omega)^2 \mathbf{I} + (1 - ih) \mathbf{K}) \chi_{\beta j} &= (\mathbf{f}_{Ej} + (j\omega)^2 \mathbf{M} \chi_{\beta j}) \delta(x - L_E) \quad x \in x_\beta \\ \mathbf{L} \dot{\chi}_{\beta j} &= 0 \quad x = L \\ \mathbf{f}_{lj} &= \mathbf{D} \chi_{\beta j} \quad x = L_c \end{aligned} \quad (23)$$

and

$$\begin{aligned}
 &(- (j\omega)^2 \mathbf{I} + (1 - ih)\mathbf{K})\chi_{\alpha_j} + \mathbf{f}_{nl,j} = \mathbf{f}_{E,j} \quad x \in x_\alpha \\
 &\mathbf{L}_j \chi_{\alpha_j} = 0 \quad x = 0 \\
 &\mathbf{f}_{E,j} = \mathbf{D}_j \chi_{\alpha_j} \quad x = L_c \\
 &\mathbf{f}_{E,j} = \begin{cases} \mathbf{f}_{E_0} & j = 0 \\ 0 & j > 0 \end{cases}
 \end{aligned} \tag{24}$$

where  $\mathbf{D} = -\mathbf{L}$  is the differential operator transforming deformation field  $\chi_j$  to internal force  $\mathbf{f}_j$ . Employing the spectral element method (details are provided in Appendix A) Eq. (23) is rearranged in the following matrix form:

$$\begin{Bmatrix} -\mathbf{f}_{jx=L_c} \\ \mathbf{f}_{E\beta_j} + \omega_j^2 \mathbf{M} \chi_{jx=L_E} \\ 0 \end{Bmatrix} = \begin{bmatrix} \mathbf{K}_{L_c L_c} & \mathbf{K}_{L_c L_E} & 0 \\ \mathbf{K}_{L_E L_c} & \mathbf{K}_{L_E L_E} + \mathbf{K}_{L_E L_E} & \mathbf{K}_{L_E L} \\ 0 & \mathbf{K}_{L_E L} & \mathbf{K}_{L L} \end{bmatrix} \begin{Bmatrix} \chi_{jx=L_c} \\ \chi_{jx=L_E} \\ \chi_{jx=L} \end{Bmatrix} \tag{25}$$

The size of the matrix Eq. (25) is reduced by eliminating its second and third rows leading to,

$$\mathbf{f}_{jx=L_c} = \mathbf{K}_{M_j} \chi_{jx=L_c} + \mathbf{f}_{ET\beta_j} \tag{26a}$$

where

$$\mathbf{f}_{ET\beta_j} = \mathbf{A}_j \mathbf{f}_{E\beta_j}, \mathbf{K}_{M_j} = -(\mathbf{A}_j \mathbf{K}_{L_c L_c} + \mathbf{K}_{L_c L_c}), \mathbf{A}_j = \mathbf{K}_{L_c L_c} (\mathbf{K}_{L_E L} \mathbf{K}_{L_E L}^{-1} \mathbf{K}_{L_E L} + \omega_j^2 \mathbf{M} - \mathbf{K}_{L_E L} - \mathbf{K}_{L_E L})^{-1} \tag{26a'}$$

Substituting Eq. (26) in Eq. (24) leads to the condensed form of the beam motion equations

$$(- (j\omega)^2 \mathbf{I} + (1 - ih)\mathbf{K})\chi_{\alpha_j} + \mathbf{f}_{nl,j} = \mathbf{f}_{E,j} - \mathbf{f}_{ET\beta_j} \delta(x - L_c) \quad x \in x_\alpha, \mathbf{L}_j \chi_{\alpha_j} = 0 \quad x = 0, (\mathbf{D}_j - \mathbf{K}_{M_j})\chi_{\alpha_j} = 0 \quad x = L_c \tag{27}$$

Subsequently, in order to find an appropriate orthogonal basis for  $\chi_{\alpha_j}$ ,  $\mathbf{K}_{M_j}$  and  $\mathbf{L}_j$  are evaluated at the frequency ( $j\omega$ ) then,

$$\begin{aligned}
 &(- \lambda_{jk}^2 \mathbf{I} + (1 - ih)\mathbf{K})\phi_{jk} = 0 \quad x \in x_\alpha, \\
 &\mathbf{L}_j \phi_{jk} = 0 \quad x = 0, \\
 &(\mathbf{D} - \mathbf{K}_{M_j})\phi_{jk} = 0 \quad x = L_c,
 \end{aligned} \tag{28}$$

is the eigenvalue problem of the linearized condensed system, and  $\phi_{jk}$  is the  $k$ th mass normalized eigen-function vector and  $\lambda_{jk}$  is its companion eigenvalue. In the case of  $j = 0$ ,  $\mathbf{K}_{M_j}$  is a zero matrix and  $h$  is set to zero for achieving real mode shapes. Finally,  $\chi_{\alpha_j}$  is approximated by few mode shapes of the condensed system in the form of,

$$\chi_{\alpha_j} \cong \Phi_j (\eta_{c_j} + \eta_{s_j}), \tag{29}$$

where  $\eta_{c_j}$  and  $\eta_{s_j}$  are unknown real vectors ( $\eta_{s_0} = 0$ ) and  $\Phi_j$  is the modal matrix in which mode shapes,  $\phi_{jk}$ , are arranged in column fashion. Substituting Eq. (29) in Eq. (27) and using the Galerkin method, the equations of motion are rewritten in the algebraic form of,

$$\begin{aligned}
 &\Theta_j (\eta_{c_j} + \eta_{s_j}) + \mathbf{f}_{nl,j}, \Phi_j + \Phi_{jx=L_c} \mathbf{f}_{ET\beta_j} = 0 \quad j > 0 \quad \Omega_0^2 \eta_{c_0} + \mathbf{f}_{nl_0}, \Phi_0 - \mathbf{f}_{E_0}, \Phi_0 = 0 \quad j = 0 \\
 &\Theta_j = (- \omega_j^2 \mathbf{M} - i\omega_j \mathbf{C} + \mathbf{K})\Phi_j, \Phi_j = (- \omega_j^2 \mathbf{I} + (1 - ih)\Omega_j^2) \quad \mathbf{a}, \mathbf{b} = \int_0^{L_c} \mathbf{b}^T \mathbf{a} dx,
 \end{aligned} \tag{30}$$

where  $\Omega_j$  is a diagonal matrix that eigenvalues of Eq. (28),  $\lambda_{jk}$ , are arranged in it with respect to  $\Phi_j$ . Solution of Eq. (30) results  $\eta_{c_j}$  and  $\eta_{s_j}$  and defines the beam motion response.

### 4.3. The contact model parameter identification

The input force and the response of system are measured in the experimental part of the work. A force residual minimization strategy is selected to identify the restoring forces in the contact by inserting the measured quantities into Eq. (30) and identifying the nonlinear contact forces. A side constraint is introduced to the force residual objective function by requiring minimum deviation between measured and predicted responses as,

$$\sum_j \left\| \Theta_j (\eta_{c_j} + \eta_{s_j}) + \left\langle \mathbf{f}_{nl_j}, \Phi_j \right\rangle + \Phi_{jx=L_c} \mathbf{f}_{ET\beta_j} \right\| + \gamma \|w_{test} - w_{modell}\|. \tag{31}$$

**Table 3**  
Identified parameters of the contact model.

Parameter	$n$	$m$	$C_p$	$C_Q$	$k_N$	$C_k$
Identified values	1.01	1.16	$27.6 \times 10^{-4}$	0.14	54.5	0.42

The L-Curve method is employed to find the regularization parameter  $\gamma$  where the details are presented in Ref. [27]. The vector  $w_{test}$  contains measured responses at the points 1 to 7 of the beam and  $w_{model}$  is the corresponding vector from the analytical model.

In this practice the parameters of the proposed contact model ( $n$ ,  $m$ ,  $C_p$ ,  $C_Q$ ,  $C_k$  and  $k_N$ ) are identified by minimizing the norm  $\|w_{test} - w_{model}\|$  for the load cases 1 and 6 simultaneously.  $w_{model}$  is calculated by direct solution of Eq. (30). The identified contact parameters are then employed to predict to responses at points 1 to 7 for other load cases (i.e. 2 to 5 and 7 to 9).

In identification procedure analytical model predictions are obtained by expanding the response up to the 6th harmonic ( $j=6$ ). This is due to observed harmonics in measurements and minimizing numerical burden; it was observed expansion of response using 9 harmonics does not change the results.

In order to evaluate the integrals of Eq. (30) numerically, 19 and 101 Gaussian Quadrature points are employed for contact region ( $0 < x < L_c$ ) and time domain ( $0 < t < T$ ) respectively. Using the Gaussian Quadrature method improved the

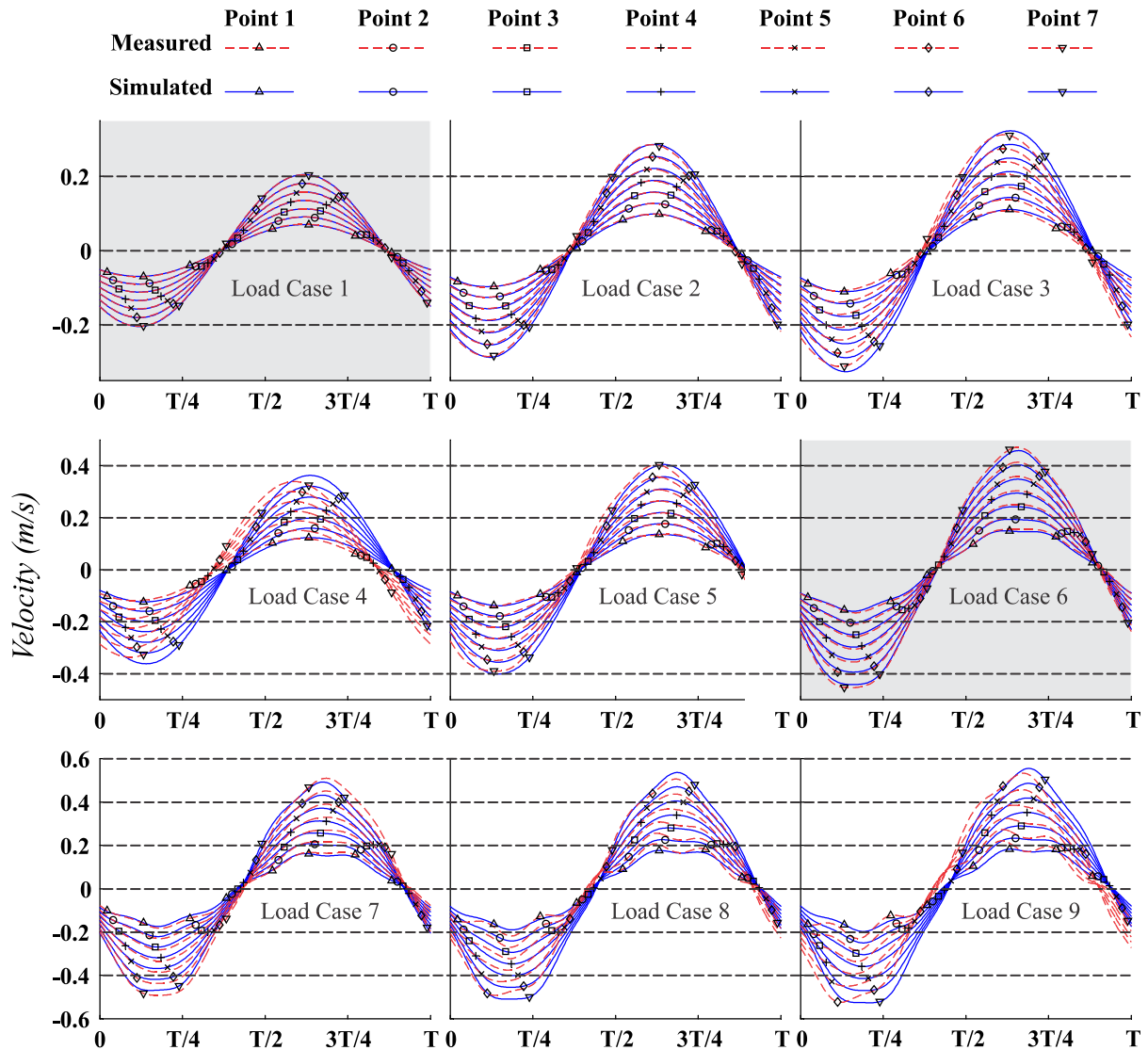


**Fig. 14.** Measured and simulated time response of experimental case study at the resonance frequencies.

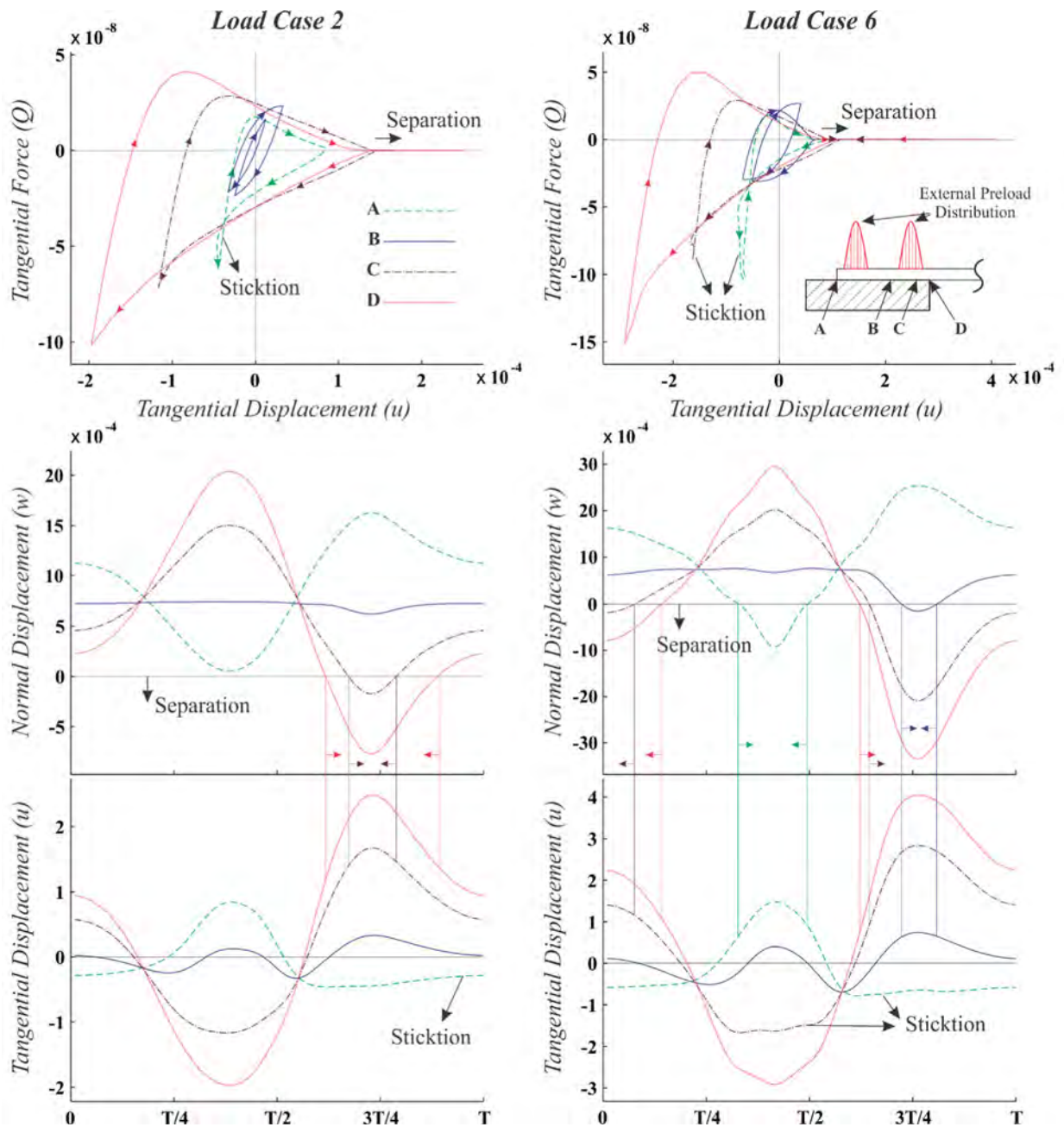


Fig. 15. Hysteresis loops along the contact at selected points.

computation speed with desired accuracy compared with other numerical integration methods.

Powell's method is selected to perform the optimization procedure with a number of initial guesses to ensure the uniqueness of the identified parameters. The identified contact parameters are shown in Table 3.

The identified value for  $n$  shows a linear relation between penetration depth and normal load, which is obvious in many contact models [8,28]. Etsion and his colleagues [11,12] reported  $m$  (see Eq. (9)) is always less than one but in this study it found 1.16. Refs. [11,12] are considering contact between a rough surface against a rigid surface under static loading condition. In the present study two rough surfaces of different materials (steel and aluminum) in contact under dynamic loading are considered. These differences contribute to the mentioned inconsistency (Table 3).

Finally, the ratio between tangential and normal stiffness is found  $C_k = 0.42$  that correlates with Baltazar et al. [29] measurements. The model responses are calculated using the identified contact model parameters and the outcomes are depicted in Fig. 14.

The predicted response for the fundamental harmonics correlate well with measured results both in magnitude and

phase; the highest discrepancy is observed in load case 4. The internal resonance is also predicted by the model. This phenomenon occurred between 1st and 6th harmonics from load case 6 onward where the excitation force was significant. The predicted magnitude and phase of 6th harmonics are in agreement with measured data for load cases 6 and 7 but the contact model behaves stiffer than the test structure for the load cases 8 and 9. In these two load cases the amplitude of measured responses are greater than the predicted ones.

Fig. 15 shows the hysteresis loops of the model for the load cases 2 and 6 at selected points along the contact, named A, B, C and D. For the load case 2, separation only occurs at the right side of the contact at the points C and D. Increasing the excitation amplitude in the load case 6, all the points along the contact experience separation during each cycle. Furthermore, increasing the excitation force level causes the vibration amplitudes grow in normal direction towards separation direction which produces the softening behavior of the contact. Also, maximum tangential displacement occurs during the separation for the selected points. The two side of the contact move with a  $\pi$  phase difference both in normal and tangential direction. The right side of the contact has maximum displacements and the left side almost stick despite movement in normal direction.

The model predictions correlate well with the observed experimental results. These show the identified values are insensitive to the measurement disturbances and may be adopted as good estimates of the parameters in mean value sense. However due to unavoidable uncertainties in the measurements and modeling, one may look for variance bounds of each parameter as well.

**5. Conclusions**

A new contact interface model considering friction and normal load variations is presented. The coupling effect between normal and tangential deformations are considered in the model which makes it capable of predicting phenomenon such as lift up in the contact interface. The model needs no integration computations and its implementation has minimum computational complexity while its predictions of the contact behavior in normal and tangential directions correlate well with several experimental case studies available in the literature. A separate experimental case study was also conducted to identify the coupling effects between shear and normal deformations. In conjunction with a reduction technique, six design variables of the proposed model are successfully identified from the experimental observations and are employed to predict the restoring force and deformations in the contact region. The identified parameters and the produced model predictions are in good agreement with experimental studies indicating the physics of frictional contact interface is well represented by the model.

**Appendix A**

The equation of motion for the beam section  $q$  shown in Fig. 16 that vibrates at frequency of  $\omega$  is (see Eq. (19))

$$(-\omega^2\mathbf{I}+(1-ih)\mathbf{K})\chi = 0 \tag{A-1}$$

A free wave that moves in this beam is in the form

$$\chi = \{a_u \ a_\phi \ a_w\}^T e^{ikx} \tag{A-2}$$

where  $k$  is the wave number and  $\{a_u \ a_\phi \ a_w\}^T$  is wave polarization vector. Substituting Eq. (A-2) in Eq. (A-1) leads to

$$\begin{bmatrix} f_u & 0 & 0 \\ 0 & f_\phi & f_{\phi w} \\ 0 & -f_{\phi w} & f_w \end{bmatrix} \begin{Bmatrix} a_u \\ a_\phi \\ a_w \end{Bmatrix} = \begin{Bmatrix} 0 \\ 0 \\ 0 \end{Bmatrix}, \tag{A-3}$$

where

$$\begin{aligned} f_u &= -\omega^2 + (1-ih)k^2, \\ f_\phi &= -\omega^2 + (1-ih)k^2 + \kappa(1-ih), \\ f_{\phi w} &= \kappa(1-ih)ik, \end{aligned}$$

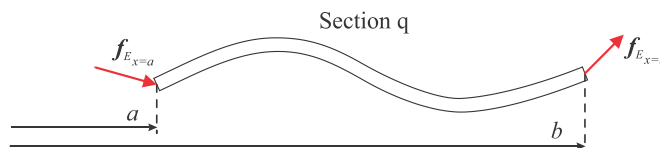


Fig. 16. A beam section vibrating at  $\omega$  frequency under two periodic external loads.

$$f_w = -\omega^2 + \kappa(1-ih)k^2.$$

Solving the eigenvalue problem of Eq. (A-3) results six wave numbers and its companion wave polarization vectors. This means there are six free waves moving along the beam ( $\mathbf{w}_i = \{a_u \ a_\phi \ a_w\}_i^T e^{ik_i x}$ ,  $i=1, 2, \dots, 6$ ). Therefore, general form of  $\chi$  in Eq. (A-1) using the free waves is written in the form

$$\chi = \mathbf{W}\mathbf{a}, \quad (\text{A-4})$$

where in  $\mathbf{W}$  each free waves,  $\mathbf{w}_i$ , are arranged in column fashion and  $\mathbf{a}$  is the wave amplitude vector. The internal forces are equal to

$$\mathbf{f}_i = \mathbf{D}\chi = \mathbf{D}\mathbf{W}\mathbf{a} \quad (\text{A-5})$$

where  $\mathbf{D} = -\mathbf{L}$  (defined in Eq. (16)) is the differential operator transforming deformation field  $\chi$  to internal forces. Using Eqs. (A-4) and (A-5) one can eliminate the wave amplitude and write

$$\begin{Bmatrix} \mathbf{f}_{Ex=a} \\ \mathbf{f}_{Ex=b} \end{Bmatrix} = \begin{bmatrix} q\mathbf{K}_{aa} & q\mathbf{K}_{ab} \\ q\mathbf{K}_{ba} & q\mathbf{K}_{bb} \end{bmatrix} \begin{Bmatrix} \chi_{x=a} \\ \chi_{x=b} \end{Bmatrix}, \quad q\mathbf{K} = \begin{bmatrix} q\mathbf{K}_{aa} & q\mathbf{K}_{ab} \\ q\mathbf{K}_{ba} & q\mathbf{K}_{bb} \end{bmatrix} = - \begin{bmatrix} (\mathbf{D}\mathbf{W})_{x=a} \\ (\mathbf{D}\mathbf{W})_{x=b} \end{bmatrix} \begin{bmatrix} \mathbf{W}_{x=a} \\ \mathbf{W}_{x=b} \end{bmatrix}^{-1}. \quad (\text{A-6})$$

$\mathbf{K}$  is the spectral element stiffness matrix of section  $q$ .

## References

- [1] S. Bograd, P. Reuss, a Schmidt, L. Gaul, M. Mayer, Modeling the dynamics of mechanical joints, *Mech. Syst. Signal Process.* 25 (2011) 2801–2826, <http://dx.doi.org/10.1016/j.ymssp.2011.01.010>.
- [2] K. De Moerlooze, F. Al-Bender, H. Van Brussel, A generalised asperity-based friction model, *Tribol. Lett.* 40 (2010) 113–130, <http://dx.doi.org/10.1007/s11249-010-9645-x>.
- [3] S. Akarapu, T. Sharp, M.O. Robbins, Stiffness of contacts between rough surfaces, *Phys. Rev. Lett.* 106 (2011) 204301–204304, <http://dx.doi.org/10.1103/PhysRevLett.106.204301>.
- [4] H. Wentzel, Modelling of frictional joints in dynamically loaded structures—a review.
- [5] M. Rajaei, H. Ahmadian, Development of generalized Iwan model to simulate frictional contacts with variable normal loads, *Appl. Math. Model.* (2014) 1–13, <http://dx.doi.org/10.1016/j.apm.2014.01.008>.
- [6] P. Flores, J. Ambrósio, J.C.P. Claro, Kinematics and Dynamics of Multibody Systems with Imperfect Joints, Springer, 2008.
- [7] Y. Song, D.M. McFarland, L.A. Bergman, A.F. Vakakis, Stick-slip interface response simulation: formulation and application of a general joint/interface element, *Comput. Model. Eng. Sci.* 10 (2005) 153.
- [8] E. Cigeroglu, N. An, C.-H. Menq, A microslip friction model with normal load variation induced by normal motion, *Nonlinear Dyn.* 50 (2007) 609–626, <http://dx.doi.org/10.1007/s11071-006-9171-4>.
- [9] K. Willner, Constitutive contact laws in structural dynamics, *Const. Comput. Model. Eng. Sci.* 48 (2009) 303–336 <<[http://www.contactmechanics.org/booklet/3\\_Willner.pdf](http://www.contactmechanics.org/booklet/3_Willner.pdf)>>. (accessed 6.01.11).
- [10] M. Ruderman, T. Bertram, Modified Maxwell-slip model of presliding friction, in: *Proceedings of the 18th IFAC World Congr.*, 2011, pp. 10764–10769.
- [11] L. Kogut, I. Etsion, A. Static, Friction model for elastic–plastic contacting rough surfaces, *J. Tribol.* 126 (2004) 34, <http://dx.doi.org/10.1115/1.1609488>.
- [12] L. Li, I. Etsion, F.E. Talke, Contact area and static friction of rough surfaces with high plasticity index, *J. Tribol.* 132 (2010) 031401, <http://dx.doi.org/10.1115/1.4001555>.
- [13] C. Campañá, B.N.J. Persson, M.H. Müser, Transverse and normal interfacial stiffness of solids with randomly rough surfaces, *J. Phys. Condens. Matter* 23 (2011) 085001, <http://dx.doi.org/10.1088/0953-8984/23/8/085001>.
- [14] D. Goerke, K. Willner, Normal contact of fractal surfaces—experimental and numerical investigations, *Wear* 264 (2008) 589–598, <http://dx.doi.org/10.1016/j.wear.2007.05.004>.
- [15] J.-P. Arz, F. Laville, Experimental characterization of small thickness elastomeric layers submitted to impact loading, *J. Sound Vib.* 326 (2009) 302–313, <http://dx.doi.org/10.1016/j.jsv.2009.04.033>.
- [16] R. Kostek, The modelling of loading, unloading and reloading of the elastic-plastic contact of rough surfaces, *J. Theor. Appl. Mech.* 50 (2012) 509–530.
- [17] K. Willner, Elasto-plastic normal contact of three-dimensional fractal surfaces using halfspace theory, *J. Tribol.* 126 (2004) 28–33.
- [18] R. Pohrt, V.L. Popov, Normal contact stiffness of elastic solids with fractal rough surfaces, *Phys. Rev. Lett.* 108 (2012) 104301, <http://dx.doi.org/10.1103/PhysRevLett.108.104301>.
- [19] G. Adams, Contact modeling — forces, *Tribol. Int.* 33 (2000) 431–442, [http://dx.doi.org/10.1016/S0301-679X\(00\)00063-3](http://dx.doi.org/10.1016/S0301-679X(00)00063-3).
- [20] W. Sextro, Dynamical contact problems with friction: models, methods, experiments and applications, 2007.
- [21] S. Biwa, S. Nakajima, N. Ohno, On the acoustic nonlinearity of solid–solid contact with pressure-dependent interface stiffness, *J. Appl. Mech.* 71 (2004) 508, <http://dx.doi.org/10.1115/1.1767169>.
- [22] F. Al-Bender, K. De Moerlooze, Characterization and modeling of friction and wear: an overview, *Sustain. Constr. Des.* (2011) 19–28.
- [23] F. Al-Bender, K. Moerlooze, P. Vanherck, Lift-up hysteresis butterflies in friction, *Tribol. Lett.* 46 (2012) 23–31, <http://dx.doi.org/10.1007/s11249-012-9914-y>.
- [24] Y. Zhang, I. Sharf, Validation of nonlinear viscoelastic contact force models for low speed impact, *J. Appl. Mech.* 76 (2009) 051002.
- [25] L. Li, A. Ovcharenko, I. Etsion, F. Talke, The effect of asperity flattening during cyclic normal loading of a rough spherical contact, *Tribol. Lett.* 40 (2010) 347–355, <http://dx.doi.org/10.1007/s11249-010-9672-7>.
- [26] K. De Moerlooze, F. Al-Bender, On the relationship between normal load and friction force in pre-sliding frictional contacts. Part 2: experimental investigation, *Wear* 269 (2010) 183–189, <http://dx.doi.org/10.1016/j.wear.2010.02.008>.
- [27] M. Mohammadali, H. Ahmadian, Efficient model order reduction for dynamic systems with local nonlinearities, *J. Sound Vib.* 333 (2014) 1754–1766, <http://dx.doi.org/10.1016/j.jsv.2013.11.006>.
- [28] B. Yang, M. Chu, C. Menq, Stick–slip–separation analysis and non-linear stiffness and damping characterization of friction contacts having variable normal load, *J. Sound Vib.* 210 (1998) 461–481, <http://dx.doi.org/10.1006/jsvi.1997.1305>.
- [29] A. Baltazar, S.I. Rokhlin, C. Pecorari, On the relationship between ultrasonic and micromechanical properties of contacting rough surfaces, *J. Mech. Phys. Solids* 50 (2002) 1397–1416, [http://dx.doi.org/10.1016/S0022-5096\(01\)00119-3](http://dx.doi.org/10.1016/S0022-5096(01)00119-3).